A Theory-Based Hydrometeor Identification Algorithm for X-Band Polarimetric Radars

BRENDA DOLAN AND STEVEN A. RUTLEDGE

Department of Atmospheric Science, Colorado State University, Fort Collins, Colorado

(Manuscript received 18 August 2008, in final form 29 April 2009)

ABSTRACT

Although much work has been done at S band to automatically identify hydrometeors by using polarimetric radar, several challenges are presented when adapting such algorithms to X band. At X band, attenuation and non-Rayleigh scattering can pose significant problems. This study seeks to develop a hydrometeor identification (HID) algorithm for X band based on theoretical simulations using the T-matrix scattering model of seven different hydrometeor types: rain, drizzle, aggregates, pristine ice crystals, low-density graupel, high-density graupel, and vertical ice. Hail and mixed-phase hydrometeors are excluded for the purposes of this study. Non-Rayleigh scattering effects are explored by comparison with S-band simulations. Variable ranges based on the theoretical simulations are used to create one-dimensional fuzzy-logic membership beta functions that form the basis of the new X-band HID. The theory-based X-band HID is applied to a case from the Collaborative Adaptive Sensing of the Atmosphere (CASA) Integrated Project 1 (IP1) network of X-band radars, and comparisons are made with similar S-band hydrometeor identification algorithms applied to data from the S-band polarimetric Next Generation Weather Radar (NEXRAD) prototype radar, KOUN. The X-band HID shows promise for illustrating bulk hydrometeor types and qualitatively agrees with analysis from KOUN. A simple reflectivity- and temperature-only HID is also applied to both KOUN and CASA IP1 data to reveal benefits of the polarimetric-based HID algorithms, especially in the classification of ice hydrometeors and oriented ice crystals.

1. Introduction

Polarimetric radars provide a wealth of information that can be used to estimate microphysical properties within a storm. Bulk classification of hydrometeors using polarimetry can help diagnose hail cores, rain/snow transitions, regions of graupel, and strong electric fields (via vertically aligned ice crystals), among other applications (e.g., Carey and Rutledge 1998; Vivekanandan et al. 1999; Zrnic et al. 2001; Ryzhkov et al. 2005). To date, polarimetric-based hydrometeor identification (HID) algorithms have been applied to data from primarily S-band (10–11 cm) radars (Vivekanandan et al. 1999; Liu and Chandrasekar 2000; Straka et al. 2000, hereafter S00; Ryzhkov et al. 2005; Tessendorf et al. 2005).

S00 provide an extensive overview of what has been accomplished in terms of bulk hydrometeor classification, particularly at S band. Their overview presents expected variable ranges for different hydrometeor types based on previous modeling and observational work. S00 characterize a wide variety of hydrometeors in terms of polarimetric radar observables, including hail, graupel/small hail, rain, rain mixed with wet hail, snow crystals, and aggregates. A common technique for synthesizing information from polarimetric variables into a hydrometeor classification scheme is to use a fuzzy-logic-based approach (Vivekanandan et al. 1999; Liu and Chandrasekar 2000; Zrnic et al. 2001). In contrast to a simple decision tree, fuzzy logic allows for soft and overlapping boundaries that can reduce the impact of calibration and measurement errors on the classification (Liu and Chandrasekar 2000). Fuzzy logic is a multistep process in which the polarimetric radar observations are scored based on how well they fit the membership set for a given hydrometeor type (Liu and Chandrasekar 2000; Lim et al. 2005). The reader is referred to Vivekanandan

Corresponding author address: Brenda Dolan, Department of Atmospheric Science, Colorado State University, Fort Collins, CO 80523-1371.
E-mail: bdolan@atmos.colostate.edu

DOI: 10.1175/2009JTECHA1208.1

et al. (1999), Liu and Chandrasekar (2000), and Zrnic et al. (2001) for further discussion of the fuzzy logic process. It should be noted that the fuzzy-logic-based method assigns only the hydrometeor type with the highest score to the radar volume. Thus, the HID classification from fuzzy logic should be considered the dominant type at that particular location.

HID has been extended to shorter wavelength radars (C band; Baldini et al. 2005 and others). However, applying hydrometeor identification to even shorter wavelengths (e.g., X band) encounters challenges because of non-Rayleigh scattering and attenuation effects, both of which are often negligible at S band. The transition out of the Rayleigh scattering regime is strongly dependent on wavelength and hydrometeor size but also depends on hydrometeor phase resulting from the different dielectric response in ice and water to incident radiation. As such, the characteristic diameter for which Rayleigh approximations can be used decreases with decreasing radar wavelength, which results in a larger range of hydrometeors falling out of the Rayleigh regime at X band than that at S band. For example, the Rayleigh approximation can be used for water targets with diameters less than 7 mm at S band, which encompasses nearly all rain and graupel particles, with only large raindrops and hailstones falling into the Mie regime. At X band, rain diameters less than about 2 mm can be considered to be in the Rayleigh regime, resulting in large rain drops and larger graupel and small hail being Mie scatterers. Thus, direct application of an S-band HID could lead to improper categorization at shorter wavelengths.

The purpose of this study is to develop a hydrometeor identification algorithm for X band that is based on theoretical simulations of radar moments for various hydrometeor types. The theoretical simulations will be used to characterize and understand the non-Rayleigh scattering and response of meteorological targets to incident X-band radiation. The results of the simulations will be used to develop membership beta functions as part of an X-band fuzzy-logic hydrometeor identification scheme. The HID will be applied to data from the Collaborative Adaptive Sensing of the Atmosphere (CASA) Integrated Project 1 (IP1) network of X-band radars located in Oklahoma (Chandrasekar et al. 2008). Section 2 describes the theoretical simulations and results. Section 3 describes the development of the fuzzy-logic hydrometeor identification scheme and application to data from the CASA IP1 network, and the polarimetric KOUN S-band radar operated by the National Oceanic and Atmospheric Administration (NOAA) National Severe Storms Laboratory (Ryzhkov et al. 2005). Different HID algorithms are compared to determine the representativeness and utility of the theory-based X-band HID.

2. Theoretical simulations

a. Methodology

To characterize the behavior of Mie scatterers at X band (3.2 cm), the T-matrix and Mueller-matrix scattering models were used (Barber and Yeh 1975; Vivekanandan et al. 1991). The T-matrix model takes microphysical characteristics of specific hydrometeors (diameter D, axis ratio a/b, temperature T, and particle bulk density ρ) and computes the backscattering cross section at a particular incident wavelength λ. The Mueller-matrix model then calculates the radar moments (reflectivity Z_h, differential reflectivity Z_{dr}, specific differential phase K_{dp}, and correlation coefficient ρ_{hv}) for a distribution of hydrometeors in a specified volume. The microphysical properties necessary for the Mueller matrix are canting angle distribution (assumed distribution type, mean angle θ_m, and standard deviation σ), particle size distribution (distribution type, slope, and intercept), and radar elevation angle and volume.

Scattering simulations were run for seven different hydrometeor types: drizzle/light rain (DZ), rain (RN), aggregates (AG), ice crystals (CR), low-density graupel (LDG), high-density graupel/precipitation ice (HDG), and vertically aligned ice (VI). Because of the significant non-Rayleigh effects and attenuation associated with large hail at X band, this study chose to focus on the aforementioned seven hydrometeor types. An additional ''unclassified'' (UC) category was included for the case in which the HID score for all types was zero. Simulations were run at 11 cm in order to maintain a reference point against expected ranges of variable values, such as those given for S band in S00. Additionally, the Colorado State University (CSU) Radar Meteorology Group hydrometeor identification algorithm (CSUHID; discussed in Tessendorf et al. 2005) was used as a baseline for comparison with the S-band scattering simulations. S00 and CSUHID variable ranges are determined based on previous modeling studies, in situ observations, and personal experience with S-band polarimetric radar observations (e.g., Carey and Rutledge 1998; Liu and Chandrasekar 2000; S00; Lim 2001; Tessendorf et al. 2005).

Numerous scattering simulations, intended to span possible physical conditions associated with each hydrometeor type, were carried out at S and X bands (11 and 3.2 cm, respectively) by simulating a wide variety of microphysical conditions (including different temperatures, axis ratios, particle size distributions, and canting angle distributions). The resulting model output for S band was compared with S00 and CSUHID to ensure the physical representativeness of the simulated conditions. The parameters used for each of the seven hydrometeor

TABLE 1. Microphysical inputs used in the T-matrix scattering model for the seven modeled hydrometeor types.

Type	Axis ratio (a/b)	Temperature (°C)	Density (g cm^{-3})	$D_{\min}$ (mm)	$D_{\max}$ (mm)	Δd
AG	0.2, 0.9	−15.0, 5.0	0.1, 0.2, BR06,[a] H00[b]	1	12	0.1
CR	0.125, 0.15, 0.35	−40, −10	0.4, 0.9	0.05	1.5	0.005
DZ	1.0, 0.9999	0, 5, 10, 20	—	0.1	10	0.05
	1.0, 0.999, GC84	5, 20	—	0.35	0.55	0.01
HDG	0.5, 0.65, 0.75, 0.9, 1.1, 1.25	−5.0, 5.0	0.55, 0.65, 0.75, 0.85, 0.9	1	10	0.1
LDG	0.5, 0.65, 0.75, 0.9, 1.1, 1.25	−20, −10	0.25, 0.35, 0.45, 0.55	1	10	0.1
	0.65, 0.9, 1.1, 1.25	−10	0.25, 0.35, 0.45, 0.55	1	10	0.1
RAIN	CB90,[c] PP71,[d] J83,[e] BR02,[f] GC84, BC87[g]	3, 10, 20	—	0.5	10	0.05
VI	0.125, 0.15, 0.35	−40, −10	0.4, 0.9	0.05	1.5	0.005

[a] Brandes et al. (2006) size–density relationship for snow.
[b] Hogan et al. (2000) size–density relationship for snow.
[c] Chuang and Beard (1990) drop shape model.
[d] Pruppacher and Pitter (1971) drop shape model.
[e] Jameson (1983) drop shape model.
[f] Brandes et al. (2002) drop shape model.
[g] Beard and Chuang (1987) drop shape model.

types are described in the next subsection. Because differential measurements, such as Z_{dr} and K_{dp}, can depend on viewing angle, two different radar elevation angles were used: one at low elevation (1°) and one at high elevation (30°, which corresponds to the highest elevation angle scanned by the IP1 radars). A sensitivity study to demonstrate the dependence of Z_{dr} and K_{dp} on viewing angle was performed using a monodisperse population of 3-mm-diameter rain drops. Under the specified conditions, Z_{dr} changed by 0.5 dB between 1° and 30° in elevation angle, and K_{dp} changed by less than 0.1° km^{-1} between the two elevation angles for both S and X bands. Gaussian canting angle distribution was assumed, with a varying standard deviation σ. Simulations were comprised of single hydrometeor types only; no mixtures of particle types were simulated.

b. Simulation microphysics

The T-matrix input parameters outlined below for the seven hydrometeors are summarized in Table 1, and the Mueller-matrix microphysical parameters are aggregated in Table 2. The dielectric factor $|K|^2$, which is used in the scattering calculations, is represented as

$$|K|^2 = \left|\frac{(m^2-1)}{(m^2+2)}\right|^2, \quad (1)$$

where m is the complex index of refraction,

$$m = n + ik. \quad (2)$$

Here, n is the ordinary refractive index and k is the absorption coefficient; n and k are dependent on temperature, density, and wavelength (Battan 1973). For ice–air mixtures (such as aggregates), the ratio K/ρ is assumed to be constant (Battan 1973).

1) RAIN

Although the microphysical characteristics of rain are probably the best understood of all hydrometeor types, questions still remain about drop axis ratio relationships and size distributions. A wide variety of drop shape models have been suggested to describe the shape of falling large raindrops (Pruppacher and Beard 1970; Pruppacher and Pitter 1971; Jameson 1983; Goddard and Cherry 1984, hereafter GC84; Beard and Chuang 1987; Chuang and Beard 1990; Brandes et al. 2002; and others). Six different axis ratio relationships were chosen for use in this study: Pruppacher and Pitter (1971), GC84, Jameson (1983), Beard and Chuang (1987), Chuang and Beard (1990), and Brandes et al. (2002). Beard and Jameson (1983) and McCormick and Hendry (1974) described canting angle distributions of raindrops. Based on those findings, a truncated Gaussian distribution with a mean of 0° and σ of 1°, 4°, and 10° was used. A normalized gamma distribution (Ulbrich 1983; Willis 1984; Bringi and Chandrasekar 2001) was used for the drop size distribution:

$$N(D) = N_w f(\mu)\left(\frac{D}{D_0}\right)\exp\left[-(3.67+\mu)\frac{D}{D_0}\right], \quad (3)$$

where D_0 is the median volume diameter, μ is the shape parameter, both $N(D)$ and N_w have units of mm^{-1} m^{-3}, and

$$f(\mu) = \frac{6}{(3.67)^4}\frac{(3.67+\mu)^{\mu+4}}{\Gamma(\mu+4)}. \quad (4)$$

Rain rates R calculated from the gamma distribution were used to limit the retrieval to $2.5 < R < 300$ mm h^{-1} (Chandrasekar et al. 2006).

TABLE 2. Microphysical parameters used in the Mueller-matrix calculation of radar variables from scattering simulations.

Type	θ_m (°)	σ (°)	Distribution type	μ	Rain rate (mm h^{-1})	D_0 (mm)	Elevation angle (°)	N_0 (cm^{-1} m^{-3})	Total No. simulations
AG	0	15, 30	Exponential	—	0.5, 10.	—	1, 30	—	128
CR	0	15, 30	Exponential	—	0.01, 0.1, 10	—	1, 30	0.05, 0.055, 0.04, 0.035	144
DZ	0	1	Monodisperse	—	—	0.1	1, 30	80 000	256
	0	0.1, 1, 4	Exponential	—	0.1, 0.5, 1.0, 2.0, 2.5	—	1, 30	80 000	900
HDG	0	10, 20	Eq. (7)	—	—	0.3, 0.4, 0.5, 0.55, 0.65, 0.7, 0.75	1, 30	Eq. (7)	1680
LDG	0	10, 20	Eq. (7)	—	—	0.15, 0.2, 0.3, 0.45, 0.5	1, 30	Eq. (7)	960
	0	10, 20	Exponential	—	—	0.15, 0.2, 0.1, 0.25	1, 30	80 000	128
RN	0	1, 4, 10	Normalized gamma	−0.1, 1.0, 2.0, 3.0, 4.0	—	0.05, 0.1, 0.15, 0.2, 0.25, 0.3, 0.35	1, 30	1000, 5000, 10 000, 50 000, 100 000	14 580
VI	90	15, 30	Exponential	—	0.01, 0.1, 10.	—	1, 30	0.05, 0.055, 0.04, 0.035	144

2) DRIZZLE/LIGHT RAIN

Drizzle was modeled using a monodisperse population of droplets. Simulations with diameters from 0.3 to 0.55 mm were calculated at temperatures ranging from 0° to 20°C. The very small size of the drops results in little deformation due to drag forces, so spherical axis ratios were used. The drizzle category is also intended to capture light rain, below the 2.5 mm h^{-1} rain rate threshold used in the rain simulations. For simulations of light rain, the GC84 drop axis ratio was assumed and a simple Marshall–Palmer exponential particle size distribution was used:

$$N(D) = N_0 \exp(-\Lambda D) \tag{5}$$

where N_0 was assumed to be 80 000 cm^{-1} m^{-3} and Λ (mm^{-1}) is related to the rain rate by

$$\Lambda = 4.1\mathrm{R}^{-0.21}. \tag{6}$$

Rain rates between 0.1 and 2.5 mm h^{-1} were simulated for light rain.

3) LOW-DENSITY GRAUPEL

The bulk microphysical characteristics of graupel are less certain. For example, the bulk density of graupel reported in the literature ranges from 0.05 g cm^{-3} (Locatelli and Hobbs 1974) up to >0.7 g cm^{-3} (List 1958; Braham 1963; Zikmunda and Vali 1972; Heymsfield 1978). For the low bulk density category, densities of >0.25 and ≤0.55 g cm^{-3} were considered, which is consistent with the findings of a number of studies (Fletcher 1962; Zikmunda and Vali 1972; Locatelli and Hobbs 1974; Pruppacher and Klett 1997; Heymsfield et al. 2004). Additionally, there are a variety of shapes for graupel (conical, lump, and hexagonal; Locatelli and Hobbs 1974; Heymsfield 1978). Axis ratios between 0.65 and 1.25 were used (Heymsfield 1978; Pruppacher and Klett 1997). As noted by Aydin and Seliga (1984), axis ratios of graupel can be larger than unity. Observations by Zikmunda and Vali (1972) showed that conical graupel particles could oscillate around the vertical with amplitudes up to 20°, although studies by List and Schemenauer (1971) showed that higher-amplitude oscillations could occur with larger graupel sizes. A Gaussian canting angle distribution of graupel with standard deviations of 10° and 20° was used in this study.

The size distribution of graupel particles is also difficult to characterize. Many studies have found graupel distributions can be modeled with exponential distributions [Eq. (5); Pruppacher and Klett 1997]. Cheng and English (1983) derived an exponential relationship between the shape parameter and the slope intercept:

$$N_0 = A\Lambda^B, \tag{7}$$

where $A = 115$, $B = 3.63$, N_0 (m^{-3} mm^{-1}), and Λ (mm^{-1}).

A relationship between D_0 and Λ was assumed to be (Doviak and Zrnic 1993)

$$D_0 = \frac{3.67}{\Lambda}, \tag{8}$$

where D_0 was varied between 2 and 5 mm (Cheng and English 1983; Xu 1983) and the respective N_0 and Λ values were calculated. For smaller mean diameters of 1.5–2.5 mm, the exponential distribution was used with N_0 set to a constant 80 000 cm^{-1} m^{-3} (Xu 1983).

Low-density graupel is expected in relatively cold regions of storms; thus, temperatures of −10° and −20°C were included.

4) HIGH-DENSITY GRAUPEL/PRECIPITATION ICE

Graupel growing in regions of large supercooled water contents, melting graupel, and freezing of supercooled rain are all processes that promote graupel of greater bulk density compared to LDG; thus, a high-density graupel/precipitation ice category was also included. As S00 note, graupel and small hail have similar characteristics; therefore, it may be unrealistic to distinguish between them by using radar observations. Thus, we have chosen to group these two hydrometeor types into one category. Many of the low-density graupel microphysical inputs were also used for HDG. However, HDG particles have higher densities by definition, ranging from 0.55 to 0.9 g cm^{-3} (Auer et al. 1972; Locatelli and Hobbs 1974; Heymsfield 1978). Because high-density graupel could be associated with particles as they fall through the melting layer, temperatures were allowed to extend above freezing, up to 5°C. Axis ratios used for high-density graupel were 0.5–1.25. Canting angle standard deviations for HDG were set to 10° and 20°, which is similar to LDG. The Cheng and English (1983) exponential distribution [Eq. (7)] was used for HDG, and D_0 values ranged from 3 to 7.5 mm (Cheng and English 1983; Xu 1983).

5) ICE CRYSTALS

One of the limitations of the T-matrix model is that it is unable to model complex and intricate shapes associated with ice crystals growing by vapor deposition. Rather, ice crystals are modeled as oblate spheroids, a reasonable approximation according to the findings of Matrosov (1996). Ice crystals are generally small ($D <$ 1.5 mm; Locatelli and Hobbs 1974) with small axis ratios ranging from 0.1 to 0.3 because of preferential growth along one axis during vapor deposition (Zikmunda and Vali 1972; Rottner and Vali 1974). The density of ice crystals growing by vapor deposition tends to be near that of pure ice, so ice crystal densities between 0.4 and 0.9 g cm^{-3} were simulated (Heymsfield 1972; Ono 1970). Temperatures of −10° and −40°C were used in the simulations.

Gunn and Marshall (1958) proposed a modified Marshall–Palmer relationship between number concentration and size for snow, which was later modified by Sekhon and Srivastava (1970). Sekhon and Srivastava (1970) related the snowfall rate to the exponential size distribution [Eq. (5)] via the relation

$$D_0 = 0.14R^{0.45}, \tag{9}$$

where R is the water equivalent precipitation rate (mm^{-1}) and N_0 (mm^{-1} m^{-3}) is given as

$$N_0 = 2.5 \times 10^3 R^{-0.94}. \tag{10}$$

In this case, D_0 is the equivalent melted diameter of the ice crystal in centimeters. For the purposes of this study, precipitation rates between 0.01 and 10 mm h^{-1} were included (Sekhon and Srivastava 1970).

Canting angles of snowflakes can be significant (Zikmunda and Vali 1972; Bringi and Chandrasekar 2001; Matrosov et al. 2006). Canting angles σ of 15° and 30° were used.

6) AGGREGATES

Aggregates, which are made up of a conglomeration of smaller ice crystals, were assumed to be much larger than ice crystals, with diameters ranging from 1 to 12 mm (Locatelli and Hobbs 1974). Because aggregates are formed as different ice crystals stuck together in random orientations, they were assumed to be semispherical, with axis ratios from 0.2 to 0.9 (Barthazy and Schefold 2003). Aggregates have much lower (and less certain) bulk densities than pristine ice crystals. Pruppacher and Klett (1997) report aggregate densities ranging from 0.05 to 0.5 g cm^{-3}, with the most probable densities being from 0.01 to 0.2 g cm^{-3}. Previous studies have suggested that the bulk density varies with particle diameter. Brandes et al. (2006) suggest the following relationship between particle bulk density and particle diameter for rimed and unrimed snowflakes:

$$\rho = 0.178D^{-0.922}, \tag{11}$$

where D is the diameter of the particle in millimeters.

A density–size relationship suggested by Hogan et al. (2000) for irregular crystals and aggregates was also used:

$$\rho = 0.175D^{-0.66}. \tag{12}$$

For aggregate simulations, both fixed (0.1–0.2 g cm^{-3}) and size-dependent relationships [Eqs. (11) and (12)] for density were used.

The particle size distribution suggested by Sekhon and Srivastava (1970) was also used for aggregates [Eq. (9)], and equivalent rain rates were assumed to be 0.5–10.0 mm h^{-1}. Canting angle standard deviations of 15° and 30° were used.

Numerous studies have found that aggregation occurs most prolifically near 0°C and decreases with decreasing temperature (Hobbs et al. 1974; Rogers 1974; Willis and Heymsfield 1989). A secondary maximum in aggregation has also been observed from around −10° to −17°C, which is likely associated with the dendritic ice habit

growth regime, because dendrites are the most favorable ice crystal habit for aggregate formation (Hobbs et al. 1974; Rogers 1974; Field 1999). Magono (1954) noted that no aggregates were observed at temperatures colder than −10°C, and Hobbs et al. (1974) found that, for small particle concentrations, aggregates were unlikely to form below −15°C. More recently, Field (1999) found evidence of aggregation down to −30°C, though pristine ice crystals were dominant at temperatures below −15°C. Studies by Willis and Heymsfield (1989) also found that some large aggregates could persist to +5°C. For simulations of aggregates, temperatures of −15° and 5°C were used.

7) VERTICALLY ALIGNED ICE

Vertically aligned ice crystals can be a useful category for diagnosing regions of possible strong electric fields. Under a strong vertical electric field, small ice crystals are acted on by Coulomb forces and align themselves with the electric field. This generally results in negative specific differential phase K_{dp} values (Carey and Rutledge 1998; Ryzhkov et al. 1998; Ryzhkov and Zrnic 1998; S00). Calculations by Weinheimer and Few (1987) showed that electric fields typically occurring in thunderstorms were sufficient to align particles with major dimensions up to 1 mm and that column crystals were much more likely to align in the field than platelike crystals. To simulate vertically oriented ice, the same microphysical characteristics of ice crystals were used, except the mean canting angle was set to 90° to simulate prolate crystals.

c. Scattering simulations

Figure 1 shows the simulated and expected ranges for reflectivity (Fig. 1a), differential reflectivity (Fig. 1b), specific differential phase (Fig. 1c), and correlation coefficient (Fig. 1d) for the seven different hydrometeor categories (the maximum and minimum values are given in Tables 3–9). The results from both the X- and S-band scattering simulations are shown relative to the S-band reference values expressed in S00 and used in the CSUHID algorithm. The references ranges are used for comparison with the simulated S-band ranges to examine how well the scattering simulations captured the expected variability for the seven hydrometeor types. The other ranges shown in Fig. 1 will be discussed in section 3 regarding the fuzzy-logic HID algorithm development. It should be noted that the CSUHID does not separate aggregates from ice crystals but rather has a single "dry snow" (DS) category that encompasses these two types. As such, the variable ranges shown for CSUHID in Fig. 1 for AG and CR are associated with the DS category.

The S-band simulation ranges compare well with S00 and CSUHID for rain, indicating that the parameters used in the simulations were representative of the expected variability of rain. Interwavelength comparisons of reflectivity show that X-band simulated reflectivity has a larger maximum and smaller minimum than the S-band reflectivity for the same microphysical input parameters. This is likely because of the increased non-Rayleigh effects of particles larger than about 2 mm at X band. As anticipated, there is very little difference between S- and X-band expected minimum and maximum reflectivity values for the DZ, CR, and VI categories, which have small enough diameters to fall into the Rayleigh regime at both wavelengths. Reflectivity ranges for LDG given by S00 differ from those given by CSUHID, which are higher on average. Simulated LDG ranges for reflectivity encompass both S00 and CSUHID ranges. Simulated HDG values do not extend as low as S00, but maximum values are into the mid-50s, similar to those given by CSUHID. The differences between S00, CSUHID, and the simulations are likely due to the definitions of LDG and HDG in terms of the sizes and assumed densities of the particles but could also be a function of mixtures of particles occurring naturally versus the single particle-type simulations. Non-Rayleigh effects are also noted in LDG and HDG, as well as some minor differences in AG. Under Rayleigh assumptions, reflectivity is independent of wavelength, resulting in the same values for X and S bands. Outside the Rayleigh regime, backscattering cross section (and therefore reflectivity) depends on wavelength. In the case of rain, the X-band reflectivity values are higher than those for S band; in all of the frozen hydrometeor types, simulated X-band ranges are found to be lower than simulated S-band ranges (Fig. 1a).

The simulated ranges of Z_{dr} capture the expected S-band ranges relatively well for DZ (Fig. 1b). Values given in S00 for the Z_{dr} of RN are allowed to go up to 6 dB, whereas maximum simulated values of S-band RN Z_{dr} were on the order of 3 dB. LDG ranges for Z_{dr} are similar to those of both S00 and CSUHID. Again, S00 and CSUHID report different ranges for HDG Z_{dr} values, but simulated S-band values contain both ranges, though they extend to lower minimum values than either S00 or CSUHID. The X-band maximum Z_{dr} value is larger than the S-band values by greater than 0.5 dB in the case of RN and HDG, and a few tenths of a decibel in the cases of LDG and DZ. Maximum AG Z_{dr} values presented in S00 are slightly less than those modeled at S band, but S00 CR Z_{dr} ranges are slightly larger than those modeled at S band. CSUHID, which does not distinguish between CR and AG, shows Z_{dr} values for DS up to 6 dB. Modeled CR maximum values go up to >5 dB, similar to CSUHID values for DS and S00 values for CR. Minimum simulated Z_{dr} values for CR do not

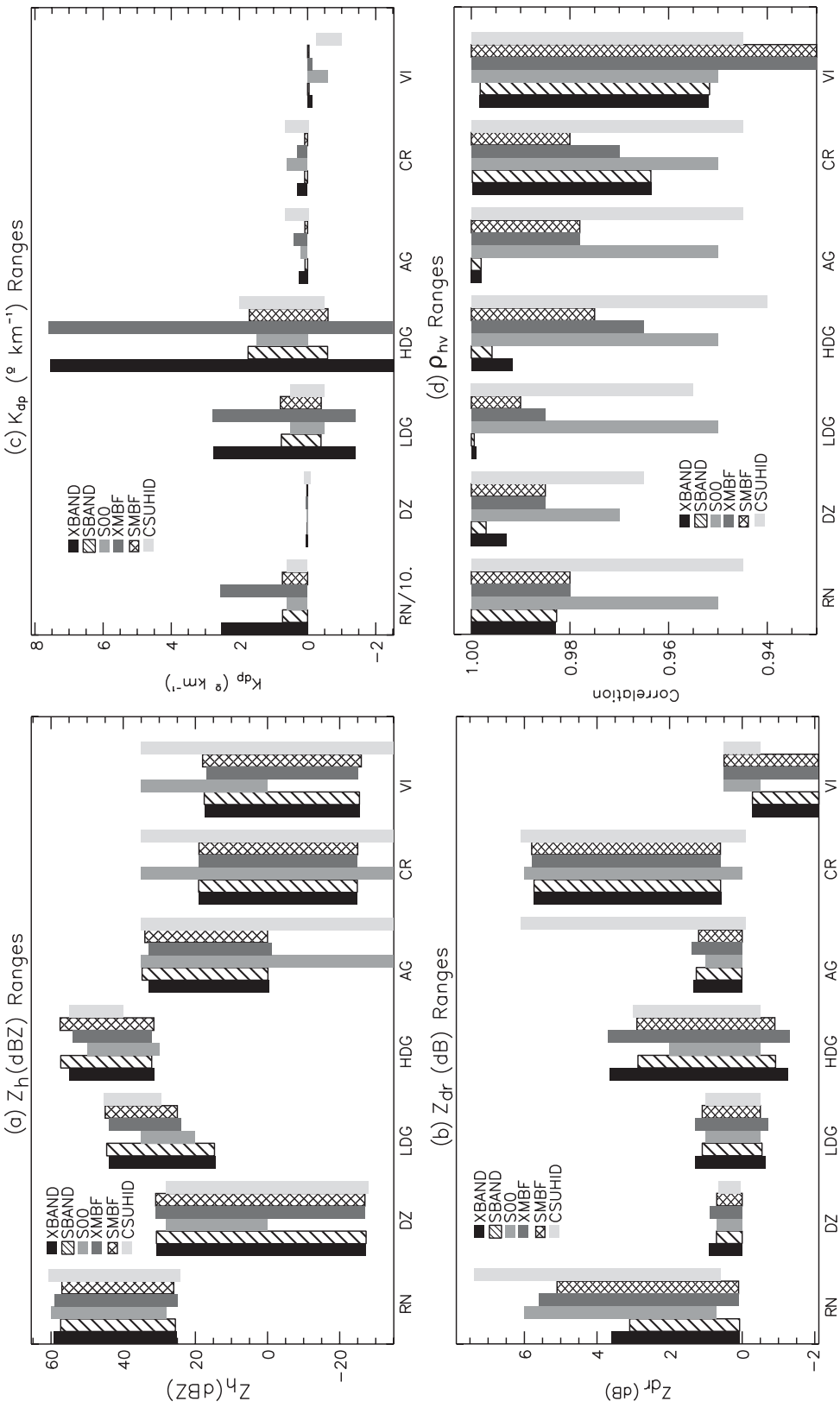

FIG. 1. Variable ranges derived from scattering simulations for seven different hydrometeor types for (a) reflectivity Z_h (dBZ) and (b) differential reflectivity Z_{dr}. Ranges for XMBF, SMBF, and CSUHID are discussed in section 3. Note that CSUHID values for AG and CR are both taken from the DS category. Shades of gray from left to right correspond to the legend values from top to bottom. (c) Specific differential phase K_{dp} and (d) correlation coefficient ρ_{hv}. Values of K_{dp} for RN are divided by 10.

TABLE 3. Radar variable maximum and minimum values for RN derived from scattering simulations (XSIM and SSIM) and S00, and values used in the MBFs for XS7 (XMBF), SS7 (SMBF), and CSUHID.

	Z_h		Z_{dr}		K_{dp}		ρ_{hv}	
	Min	Max	Min	Max	Min	Max	Min	Max
XSIM	25	59	0.07	3.6	0.004	25.5	0.983	1.0
SSIM	26	57	0.07	3.1	0.001	7.35	0.983	1.0
S00	28	60	0.7	6	0.03	6	0.95	1.0
XMBF	25	59	0.1	5.6	0.0	25.5	0.98	1.0
SMBF	26	57	0.1	5.1	0.0	7.4	0.98	1.0
CSUHID	24	61	0.6	7.4	0.05	5.95	0.945	1.0

extend to 0, as in the case of CSUHID DS and S00 CR. Modeled values of Z_{dr} for VI are strictly below 0 dB, whereas values given by S00 and CSUHID are centered around zero. As noted by Ryzhkov et al. (1998), larger particles, though less numerous, do not readily align themselves with the electric field and could increase Z_{dr} values, whereas smaller crystals align to give negative K_{dp} values (an effect not captured by the simulations).

Figure 2 illustrates the comparison between S- and X-band Z_{dr} values for all simulations of HDG, LDG, and RN. Non-Rayleigh effects at X band are evident in Z_{dr} values above 0.3 dB, where S- and X-band values deviate. The X-band Z_{dr} values are much larger, with maximum differences as S-band Z_{dr} values reach between 2 and 3 dB. This trend is captured in both rain and graupel simulations. These differences between S- and X-band Z_{dr} values are the result of non-Rayleigh scattering effects, as well as resonance effects from internal drop reflections of electromagnetic radiation that interfere with the backscattered radiation (Ryzhkov and Zrnic 2005; Matrosov et al. 2006).

Perhaps most notable are the differences in K_{dp} between S and X bands for the seven hydrometeor types. Specific differential phase is proportional to the inverse of wavelength (Bringi and Chandrasekar 2001):

$$K_{dp} = \left(\frac{180}{\lambda}\right) 10^{-3} CW(1 - \overline{r_m}), \tag{13}$$

TABLE 4. As in Table 3, but for DZ.

	Z_h		Z_{dr}		K_{dp}		ρ_{hv}	
	Min	Max	Min	Max	Min	Max	Min	Max
XSIM	−27	31	0.0	0.9	0.0	0.06	0.993	1.0
SSIM	−27	31	0.0	0.7	0.0	0.02	0.997	1.0
S00	0	28	0.0	0.7	0.0	0.03	0.97	1.0
XMBF	−27	31	0.0	0.9	0.0	0.06	0.985	1.0
SMBF	−27	21	0.0	0.7	0.0	0.02	0.99	1.0
CSUHID	−28	28	0.05	0.65	−0.1	0.1	0.965	1.0

TABLE 5. As in Table 3, but for AG.

	Z_h		Z_{dr}		K_{dp}		ρ_{hv}	
	Min	Max	Min	Max	Min	Max	Min	Max
XSIM	−0.3	33	0.0	1.3	0.0	0.3	0.9979	1.0
SSIM	−0.1	35	0.0	1.3	0.0	0.1	0.998	1.0
S00	—	<35	0.0	1.0	0.0	0.2	0.95	1.0
XMBF	−1.0	33	0.0	1.4	0.0	0.4	0.978	1.0
SMBF	0	34	0.0	1.2	0.0	0.08	0.978	1.0
CSUHID*	−35	35	−0.1	6.1	−0.05	0.65	0.945	1.0

* Values given are for DS category, which includes both ice crystals and aggregates.

where C is a wavelength-independent constant, W is the liquid water content, and $\overline{r}_m$ is the mass-weighted mean axis ratio. Thus, pure wavelength scaling would result in an increase in K_{dp} between 11 (S band) and 3.2 cm (X band) by a factor of 3.43. Figure 3 illustrates the variability of X- to S-band K_{dp} ratios observed in the simulations as a function of D_0. The X to S ratios were averaged over all simulated mean diameter D_0 for each hydrometeor type. The K_{dp} ratio for RN reaches a peak of 3.7 at mean drop diameters of 1.8 mm, and DZ ratios are larger than the expected K_{dp} ratio for all mean diameters. These results are essentially identical to Matrosov et al. (2006), who noted a K_{dp} scaling factor of 3.7 between X and S band for rain for drop diameters less than 3.5 mm. LDG and HDG show a clear increasing K_{dp} ratio with increasing mean diameter, whereas AG shows only slight deviation above the expected 3.43 ratio and VI and CR have ratios less than or close to the expected 3.43 ratio. The scattering simulations in this study show that ratios can be as large as 4.4 (HDG) and as small as 3.3 (CR and VI), depending on the assumed mean drop diameter and hydrometeor type (Fig. 3). These greater-than-expected differences in K_{dp} can be attributed to resonance and non-Rayleigh effects (Matrosov et al. 2006). It should be noted that simulated values of K_{dp} may differ slightly from observational K_{dp} values, which are derived from a highly filtered differential phase ϕ_{dp} field.

TABLE 6. As in Table 3, but for CR.

	Z_h		Z_{dr}		K_{dp}		ρ_{hv}	
	Min	Max	Min	Max	Min	Max	Min	Max
XSIM	−25	19	0.6	5.8	0.0	0.3	0.9635	0.9998
SSIM	−25	19	0.6	5.7	0.0	0.1	0.9636	0.9998
S00	—	<35	0.0	6.0	0.0	0.6	0.95	1.0
XMBF	−25	19	0.6	5.8	0.0	0.3	0.97	1.0
SMBF	−25	19	0.0	5.8	0.0	0.09	0.98	1.0
CSUHID*	−35	35	−0.1	6.0	−0.05	0.65	0.945	1.0

* Values given are for DS category, which includes both ice crystals and aggregates.

TABLE 7. As in Table 3, but for LDG.

	Z_h		Z_{dr}		K_{dp}		ρ_{hv}	
	Min	Max	Min	Max	Min	Max	Min	Max
XSIM	14	44	−0.7	1.3	−1.4	2.8	0.999	1.0
SSIM	15	45	−0.5	1.1	−0.4	0.8	0.999	1.0
S00	20	35	−0.5	1.0	−0.5	0.5	0.95	1.0
XMBF	24	44	−0.7	1.3	−1.4	2.8	0.985	1.0
SMBF	25	45	−0.5	1.1	−0.4	0.8	0.99	1.0
CSUHID	30	46	−0.5	1.00	−0.5	0.5	0.955	1.0

TABLE 9. As in Table 3, but for VI.

	Z_h		Z_{dr}		K_{dp}		ρ_{hv}	
	Min	Max	Min	Max	Min	Max	Min	Max
XSIM	−25	17	−2.1	−0.3	−0.1	0.0	0.9518	0.9983
SSIM	−25	18	−2.1	−0.3	−0.04	0.0	0.9517	0.9982
S00	—	<35	−0.5	0.5	−0.6	0.0	0.95	1.0
XMBF	−25	32	−2.1	0.5	−0.15	0.0	0.93	1.0
SMBF	−26	32	−2.1	0.5	−0.04	0.0	0.93	1.0
CSUHID	−35	35	−0.5	0.5	−1.0	−0.25	0.945	1.0

Many studies have investigated non-Rayleigh effects at X band as a function of drop size for rain (Tian et al. 2002; Ryzhkov and Zrnic 2005; Matrosov et al. 2006). To better understand non-Rayleigh effects in ice hydrometeors, a series of monodisperse simulations of HDG for single diameters ranging from 2 to 10 mm were simulated with an axis ratio of 0.7, a bulk density of 0.7 g cm^{-3}, and a temperature of −5°C (Fig. 4). For diameters below about 6 mm, reflectivity differences between S and X band are less than 1 dBZ. As the diameter increases, differences amplify up to 3.2 dBZ at a diameter of 10 mm with X-band reflectivity consistently lower than S-band reflectivity. However, large sizes of graupel only compose a small portion of the natural size distribution resulting in smaller differences (1–2 dBZ) for a distribution of particle sizes. Differential reflectivity differences between the two wavelengths increase with increasing diameter but remain generally small (<0.5 dB), with X-band Z_{dr} larger than in S band. The K_{dp} ratios are all larger than the 3.4 dictated by wavelength scaling, increasing to greater than 4.0 for diameters greater than 6 mm, reaching a maximum ratio of 4.7 at 10 mm.

It is clear from comparison with S00 and CSUHID values that the scattering simulations did not capture the full variability of ρ_{hv} (Fig. 1d). A number of factors can decrease ρ_{hv}, including mixtures of hydrometeor types and hydrometeor shape irregularities (Balakrishnan and Zrnic 1990), factors that were not modeled in the simulations. Although the ranges of values for ρ_{hv} were not completely simulated, non-Rayleigh effects can still be noted in the simulations (Fig. 1d). The copolar correlation coefficient is influenced by backscattering differential phase, which is wavelength dependent. The X-band RN ρ_{hv} values are slightly higher than S band. HDG, LDG, and DZ ranges show the opposite trend, where X-band values are slightly lower than S-band values. Low values of ρ_{hv} for VI were modeled for both X and S bands, with maximum values not extending to 1.0. This is likely due to the canting angle distribution used, with a mean canting angle of 90°.

TABLE 8. As in Table 3, but for HDG.

	Z_h		Z_{dr}		K_{dp}		ρ_{hv}	
	Min	Max	Min	Max	Min	Max	Min	Max
XSIM	31	55	−1.3	3.7	−2.5	7.6	0.992	1.0
SSIM	32	57	−0.9	2.9	−0.6	1.7	0.996	1.0
S00	30	50	−0.5	2.0	0.0	1.5	0.95	1.0
XMBF	32	54	−1.3	3.7	−2.5	7.6	0.965	1.0
SMBF	32	58	−0.9	2.9	−0.6	1.7	0.975	1.0
CSUHID	40	55	−0.5	3.0	−0.5	2.0	0.94	1.0

3. Hydrometeor identification algorithm

a. Fuzzy-logic development

The variable ranges associated with each hydrometeor type derived from the scattering simulations were used as the basis for a theory-based fuzzy-logic HID. The fuzzy-logic method employed in this study uses one-dimensional membership beta functions (MBFs) to calculate a score that describes how well the observations characterize each hydrometeor type. MBFs (β) are defined in terms of their width a, midpoint m, and slope b:

$$\beta = \frac{1}{1 + \left[\left(\frac{x-m}{a}\right)^2\right]^b}, \tag{14}$$

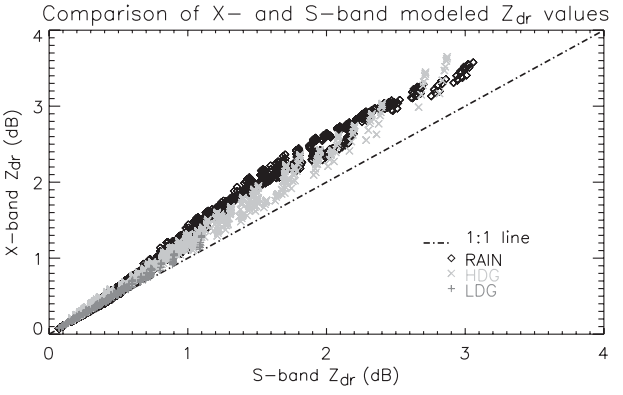

FIG. 2. The S-band versus X-band Z_{dr} values for simulations of rain (black), HDG (light gray), and LDG (medium gray). The dashed–dotted line represents a 1:1 line.

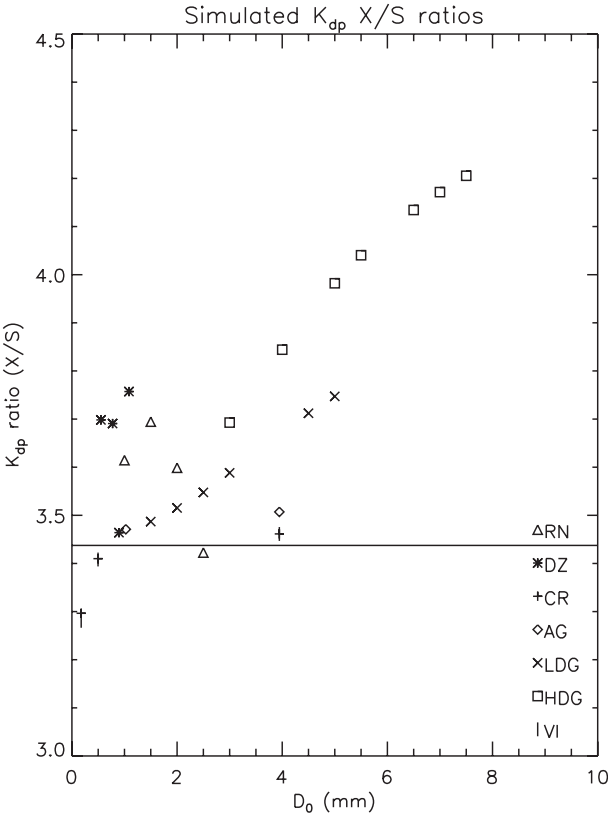

FIG. 3. Simulated K_{dp} ratios (X/S) between X and S bands for the seven hydrometeor categories as a function of median drop diameter D_0. The thick black line denotes the 3.43 ratio expected by pure wavelength scaling.

where x is the observational data value. The difference between the maximum and minimum simulation values divided by 2 gives a, whereas the width added to the minimum simulation value results in b. The slope was used to represent the confidence in the MBFs. For example, because ρ_{hv} was not well modeled by the simulations, b was generally set to a small number resulting in a wider slope to indicate the lack of confidence in the exact ranges of variables expected. For the HID algorithm, β is calculated for each variable and then multiplied by a weight, and the result for each variable is then added together to define a score associated with each hydrometeor. The hydrometeor with the highest score is determined to be the dominant hydrometeor within the observed volume.

The HID algorithm was applied to IP1 and KOUN data collected on 10 June 2007. Direct conversion of the simulated data (described earlier) into MBFs resulted in discontinuous classification with excessive amounts of LDG and little HDG and VI (not shown). This is likely due to the overlap between beta functions for frozen hydrometeor types, particularly AG, CR, HDG, and LDG. Overlap is not unexpected, given the similar microphysics (i.e., temperatures, densities, and sizes) of certain frozen hydrometeors that may not be distinguishable in the radar observations, as well as some variability not captured by the scattering simulations. Thus, modifications to the MBFs based on comparisons with S00 and CSUHID values, as well as understanding of the relative X- and S-band scattering differences, were made in order to decrease the ambiguity between hydrometeor types. Specifically, the minimum LDG values were increased from 14 to 20 dBZ, which is between the minimum values given by CSUHID and S00. Because of a large overlap between HDG and RN, S-band RN Z_{dr} values were increased to 5 dB (closer to those reported by S00), and the relative differences between X and S bands were preserved, so X-band values were increased to 5.5 dB. As discussed earlier, VI Z_{dr} observations could be dominated by larger crystals or plates that do not readily align in an electric field (a physical process not captured by the simulations); thus, Z_{dr} values for VI were increased to a maximum of 0.5 dB. Because comparison with S00 and CSUHID ranges indicate that the full variability of ρ_{hv} was not represented by the simulations, ρ_{hv} minimum values were decreased for all categories except VI, where the maximum value was increased to 1.0. Again, the relative differences between X and S bands resulting from complex non-Rayleigh scattering were preserved. The modified simulation ranges for X- and S-band MBFs (XMBF and SMBF) used in the HID are illustrated in Fig. 1. We consider these modifications appropriate to the extent that the definitions of dry graupel, wet graupel, and aggregates are somewhat overlapping, and the simulations include only single hydrometeor types, whereas observed radar volumes are likely mixtures of particles, which could alter observed ranges. Actual values used for the MBFs, as well as the simulated maxima and minima, can be found in Tables 3–9.

Several different versions of the HID were used to study the representativeness of the theory-based HID. The fuzzy-logic methodology described above was applied to all HID algorithms used in this study; the difference between each algorithm is simply due to the MBF parameters, variable weights, and variables used in the scoring process. Three HID algorithms were applied to the S-band KOUN data: the 6-category CSUHID (CSUHIDS 6); the theory-based 7-category HID with the modifications described earlier, where the MBFs were based on the theoretical simulations (SS7); and a simple reflectivity and temperature only-based HID, where the weights of the polarimetric variables were set to 0 in the fuzzy sets (ZTS). Two algorithms were run on X-band IP1 data: the modified theory-based HID (XS7)

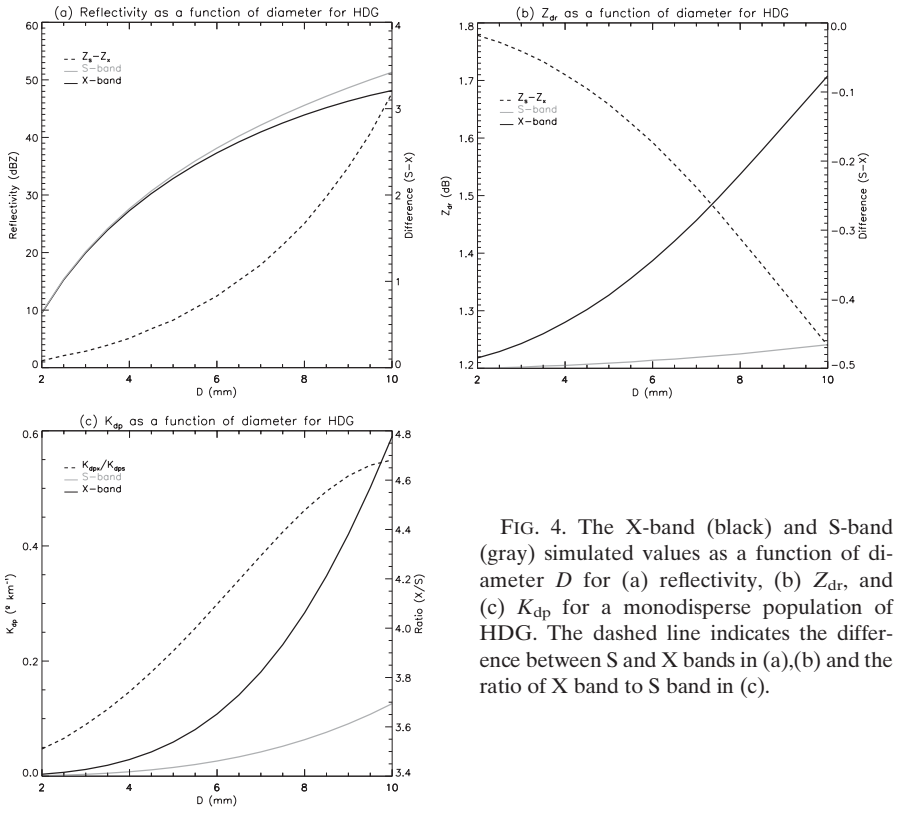

FIG. 4. The X-band (black) and S-band (gray) simulated values as a function of diameter D for (a) reflectivity, (b) Z_{dr}, and (c) K_{dp} for a monodisperse population of HDG. The dashed line indicates the difference between S and X bands in (a),(b) and the ratio of X band to S band in (c).

and a simplified X-band reflectivity and temperature HID (ZTX). The five HID algorithms are summarized in Table 10.

b. Application of algorithm

To compare the results of the X-band hydrometeor identification algorithm with more widely used S-band algorithms (and for comparison with an essentially nonattenuating wavelength), data from the CASA IP1 radar network were used in conjunction with S-band polarimetric data from the nearby NOAA/National Severe Storms Laboratory KOUN radar (approximately 75 km northeast of the center of the IP1 network). The KOUN radar scans 360° full volumes with 13 elevation angles up to 19.5° approximately every 5 min. The half-power beamwidth of KOUN is 1°. IP1 has a half-power beamwidth of 1.8° with variable scanning strategy (variable sector sizes, up to 12 elevation angles per 3-min cycle and a maximum elevation angle of 30°). A case from 10 June 2007 was chosen based on its location within the IP1 network and relatively low amounts of hail identified by a 9-category CSUHID algorithm run on KOUN, which includes small hail and large hail categories (not shown).

The radar data were first gridded to a common grid centered in the IP1 network (KOUN data to 1 km^3 and IP1 data to 0.5 km^3), then the fuzzy-logic HID was applied. In the case of the IP1 radars, the individual radar measurements were mosaicked into a single grid by taking the highest value for each variable from the available radars at individual grid points. The HID algorithms were then applied to mosaicked gridded data. The IP1 reflectivity data were corrected for attenuation using the network-based attenuation correction algorithm described in Chandrasekar and Lim (2008) and a self-consistent differential phase–based attenuation correction (Park et al. 2005) was applied to Z_{dr} values. During the IP1 2007 project, IP1 Z_{dr} values were uncalibrated. A cross-radar Z_{dr} bias was estimated using data from a stratiform case on 20 June 2007. The radar biases were then applied before data were mosaicked. Because of lower-quality Z_{dr} and ρ_{hv} data during the 2007 experiment, the weights for Z_{dr} and ρ_{hv} for the IP1 HIDs were set low (0.4 and 0.2, respectively) compared to the weight given to reflectivity (1.5), K_{dp} (1.0), and temperature (0.5) for the fuzzy-logic process. The temperature used in the HID algorithms was derived for each grid height from the local 1200 UTC Norman, Oklahoma, sounding. The melting level from the sounding was at 4.3 km MSL.

For various reasons, such as range, resolution, coverage, beam geometry, and of course wavelength, quantitative

TABLE 10. Summary of HIDs used in this study. All HIDs use the same fuzzy-logic methodology, but they differ in the MBFs as well as hydrometeor types and variables included.

HID name	Description	Hydrometeor types included	Radar data used	Source
CSUHIDS 6	S-band algorithm used at CSU in Radar Meteorology Group	DZ, RN, DS, LDG, HDG, VI	KOUN	Carey and Rutledge (1998), Liu and Chandrasekar (2000), S00, Lim (2001), and Tessendorf et al. (2005)
SS7	Theory-based S-band HID	DZ, RN, AG, CR, LDG, HDG, VI	KOUN	Theoretical simulations of hydrometeors at 11 cm described in section 2
ZTS	Fuzzy-logic-based reflectivity and temperature classification	DZ, RN, AG, CR, LDG, HDG, VI	KOUN	Same as SS7, but without Z_{dr}, K_{dp}, and ρ_{hv}
XS7	Theory-based X-band HID	DZ, RN, AG, CR, LDG, HDG, VI	IP1	Theoretical simulations of hydrometeors at 3.2 cm described in section 2
ZTX	Fuzzy-logic-based reflectivity and temperature classification	DZ, RN, AG, CR, LDG, HDG, VI	IP1	Same as XS7, but without Z_{dr}, K_{dp}, and ρ_{hv}

intercomparisons between KOUN and IP1 HIDs were of little utility. However, intrawavelength quantitative comparisons between HID algorithms applied to each dataset (KOUN and IP1) are possible and can be used to reveal differences between the theory-based HID, the simple reflectivity- and temperature-only HID, and the original S-band HID (CSUHID). Quantitative similarities between KOUN theory-based HID (SS7) and CSUHIDS 6 will lend confidence to both the X- and S-band theory-based HID algorithms. Qualitative comparisons between KOUN and IP1 data can also be made to ensure consistency in microphysical characteristics identified by the HID algorithms because no aircraft data are available for validation.

The different HID algorithms were applied to gridded IP1 and KOUN data from 10 June 2007 during an intense period of a multicellular storm. Vertical cross sections at 2347 UTC through a strong reflectivity core (located at $x = 7.0$ km in the grid coordinates) illustrate the performance of the new theory-based algorithms compared to CSUHIDS 6, as well as temperature- and reflectivity-only HIDs (Figs. 5, 6). The theory-based S-band algorithm (SS7; Fig. 5a) shows relatively the same HDG and LDG trends as CSUHIDS 6 (Fig. 5b), with a region of HDG associated with the reflectivity core (Fig. 7a), surrounded by LDG. SS7 appears to identify more HDG, LDG, and VI than CSUHIDS 6. SS7 shows a clear distinction between CR and AG around the height of the −20°C layer (~8 km), adding information about storm microphysics to the otherwise large area of dry snow identified by CSUHIDS 6. CR is identified in the cold upper regions of the storms as expected, with AG occurring closer to the melting layer, which is also physically realistic (Willis and Heymsfield 1989). The qualitative similarities between CSUHIDS 6 and SS7 lend some degree of confidence to the ability of the theory-based HID algorithms to distinguish bulk regions of hydrometeors. The IP1 theory-based HID (XS7; Fig. 6a) shows similar structure to that observed with the S-band HIDs. Common features reveal rain above the melting layer (supercooled rain lofted by strong updrafts), which aids in the formation of the surrounding HDG through accretion and riming. A large region of LDG can be seen above the layer of HDG, though the areas of graupel are much larger in XS7 than in SS7 or CSUHIDS 6. XS7 also shows some CR falling through the AG layer below −20°C. In general, XS7 qualitatively shows the same features as the KOUN classifications. The categorizations are supported by visual inspection of the radar variables (Figs. 7, 8) used in the HID. RN grid points above the melting layer are associated with large Z_h, Z_{dr}, and K_{dp} values in both the KOUN and IP1 data (Figs. 7a–c, 8a–c), indicating large, flattened drops, whereas HDG is characterized by smaller Z_{dr} but still large K_{dp} values. The distinction between HDG and LDG is made as reflectivity decreases along with small Z_{dr} and near-zero K_{dp} values. Areas of VI are mainly identified through negative K_{dp} values and CR and AG are clearly distinguished by temperature, but CR is also identified through low reflectivity paired with higher Z_{dr}. Interestingly, many of the wavelength dependencies found in the scattering simulations are realized in the data presented in Figs. 7 and 8. In the main rain core, X-band Z_{dr} values are greater than 1 dB higher than the corresponding S-band values (Figs. 7b, 8b), and K_{dp} values are approximately 3 times larger in the IP1 data than KOUN (Figs. 7c, 8c). The ρ_{hv} values are also lower at X band than at S band (Figs. 7d, 8d), particularly in the areas identified as HDG, an effect also noted in the simulations. These qualitative inspections of the data

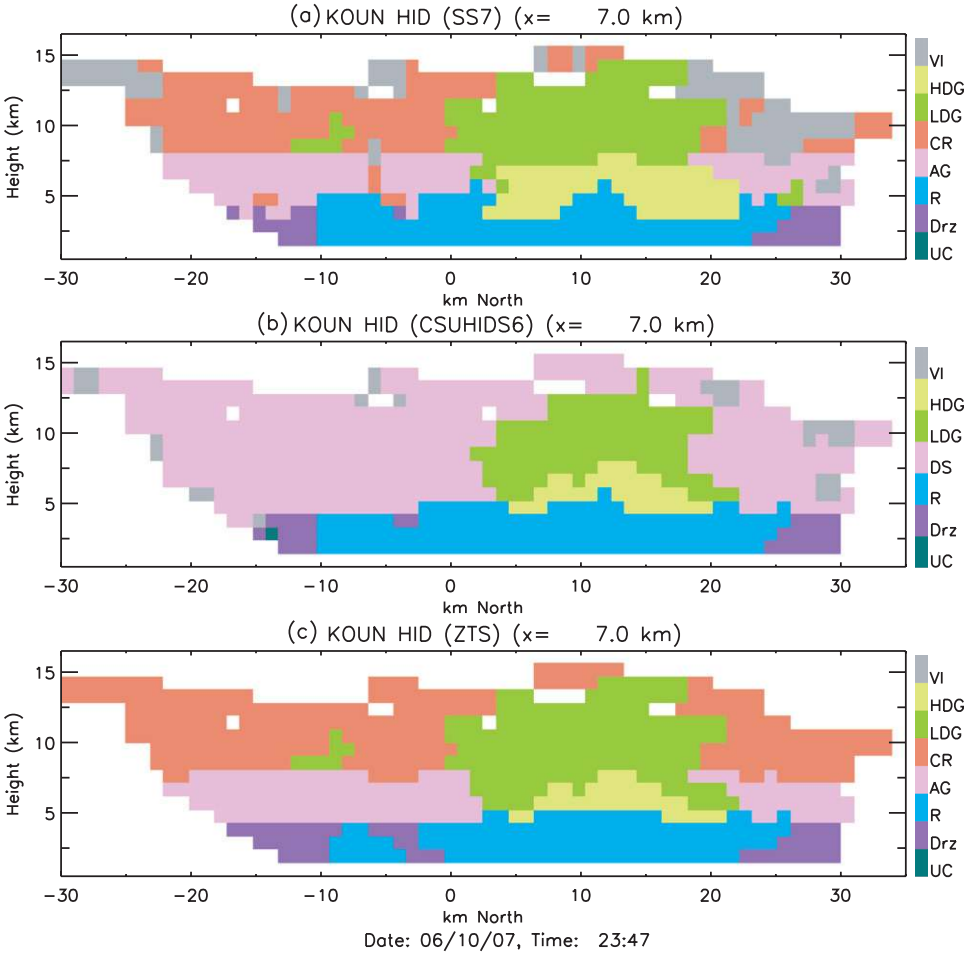

FIG. 5. A vertical cross section of gridded KOUN data at 2347 UTC 10 Jun 2007 taken through an intense part of the storm at $x = 7.0$ km in the grid coordinates. Cross sections illustrate (a) S-band theory-based HID (SS7), (b) CSUHIDS 6, and (c) S-band fuzzy-logic Z-T (ZTS).

and associated HIDs lend credence to the theory-based HIDs.

To understand the contribution of the polarimetric information in the classification, a simplified reflectivity–temperature-only algorithm was applied to the data. ZTS (Fig. 5c) generally demonstrates the same features as CSUHIDS 6 and SS7. There appears to be more drizzle below the melting layer in ZTS and, additionally, slightly less LDG. A rain core is not as distinct in ZTS, whereas in SS7 Z_{dr} and K_{dp} are used to identify the presence of large flattened water drops, which cannot be inferred from reflectivity and temperature alone. Finally, ZTS is unable to identify VI, whereas the polarimetric-based HIDs are able to employ negative K_{dp} values. ZTX (Fig. 6b) also has a diminished region of HDG, as well as more DZ below the melting layer than XS7. Again, the RN core is not as distinct as in XS7 because of the limited microphysical information available with only reflectivity and temperature. Though some CR extend below −20°C in ZTX, XS7 shows much more variability resulting from the additional information provided by Z_{dr} and K_{dp} on shape and water content of the ice particles. In this case, X-band polarimetric variables can contribute information for distinguishing AG from CR and RN from HDG, as well as providing a means to identify VI.

To quantify the differences between CSUHID, temperature–reflectivity-only HIDs, and theory-based HID algorithms, histograms of fractional grid volume for each hydrometeor type during the 2.5 h lifetime of the 10 June 2007 storm are shown in Fig. 9. The KOUN HIDs show similar trends (Fig. 9a), with the grid volume being dominated by snow hydrometeor types (DS and AG/CR). The percentage of graupel identified by SS7 was over 2 times greater than that identified by CSUHIDS 6, with 12% LDG and 8% HDG for SS7 and 5% LDG and 3% HDG for CSUHIDS 6. SS7 identified 3% less RN (10%) than CSUHIDS 6 (13%) but approximately the

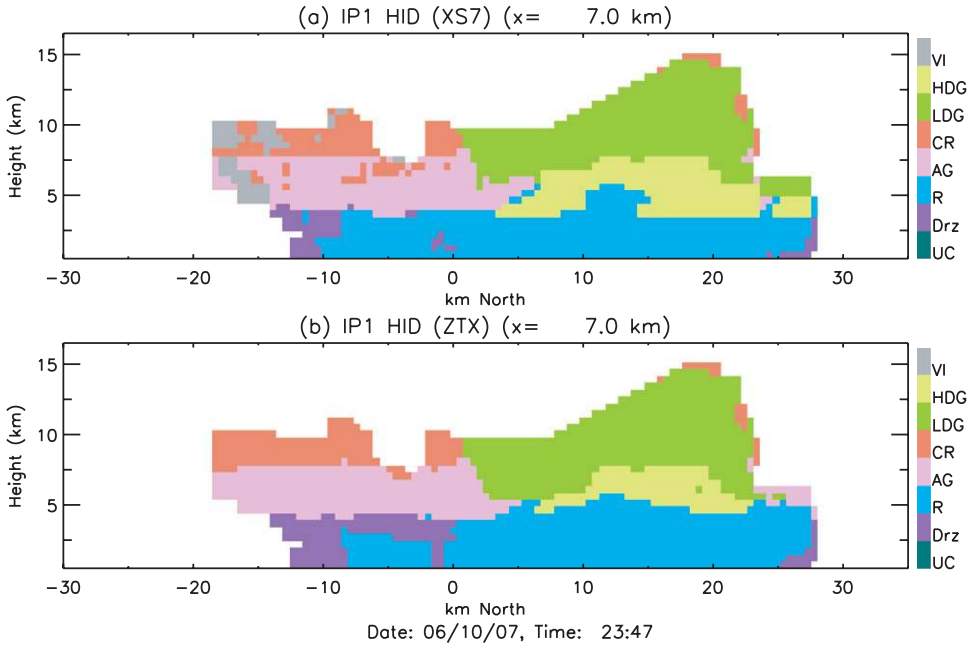

FIG. 6. A vertical cross section of gridded, mosaicked IP1 data at 2347 UTC 10 Jun 2007 taken through an intense part of the storm at $x = 7.0$ km in the grid coordinates. Cross sections illustrate (a) X-band theory-based HID (XS7), and (b) X-band fuzzy-logic Z-T HID (ZTX).

same amount of DZ (11%). For ZTS compared to CSUHIDS 6, DZ and LDG increased, HDG remained at 3%, and RN decreased from 14% to 10%. However, when compared to SS7, HDG decreased, LDG and RN were approximately the same, and AG and DZ increased. CR nearly doubled from 16% for SS7% to 31% for ZTS, likely associated with VI crystals being indistinguishable from CR by ZTS. The IP1 HIDs (Fig. 9b) classified nearly half of the grid volume as liquid hydrometeors (DZ and RN). As with the S-band HIDs, the amount of DZ increased when only temperature and reflectivity were used (30%). CR and AG amounts increased slightly for ZTX compared to XS7, whereas graupel amounts decreased.

Generally, the theory-based HID algorithms (SS7 and XS7) identified more graupel (LDG and HDG) than the CSUHID. Using only temperature and reflectivity altered the relative amounts of all seven hydrometeor types compared with the polarimetric-based algorithms, with the most significant difference being no VI identified and the relative amounts of CR and AG increasing to compensate.

Several interesting observations can be made when comparing the IP1 and KOUN histograms. First, both simulated HIDs (SS7 and XS7) identify approximately the same amount of graupel (12% LDG and 7%–8% HDG over the total volume). Second, there appears to be a much larger percentage of liquid hydrometeor types (DZ and RN) categorized on average by the IP1 HID algorithms (20%–30%) than the KOUN HID algorithms (10%–15%), and more frozen hydrometeors (VI, AG, CR, and DS) are identified by KOUN than IP1. This is likely a reflection of the coverage area and sensitivity of the different radars, not a direct artifact of the different wavelength HIDs. The IP1 radars are focused on the lowest 3 km of the atmosphere (below the melting layer during this case), resulting in the IP1 radars seeing all of the liquid hydrometeors near the surface. The sensitivity of the IP1 radars is approximately 8 dBZ at 30-km range, resulting in the light anvil regions of the storm being missed by the IP1 radars, as well as some of the upper portions of the storm because of the scanning strategy. On the other hand, because of the low-level focus of IP1 and the extended range from KOUN to the IP1 network, IP1 captures a relatively larger volume of liquid hydrometeors than KOUN. KOUN consistently scans the entire storm volume and has an approximate sensitivity of −4 dBZ over the IP1 network, resulting in a much larger quantity of frozen hydrometeors on average than the IP1 radars.

4. Conclusions

A new fuzzy-logic hydrometeor identification algorithm for X-band polarimetric radar data was developed by using scattering simulations to determine approximate

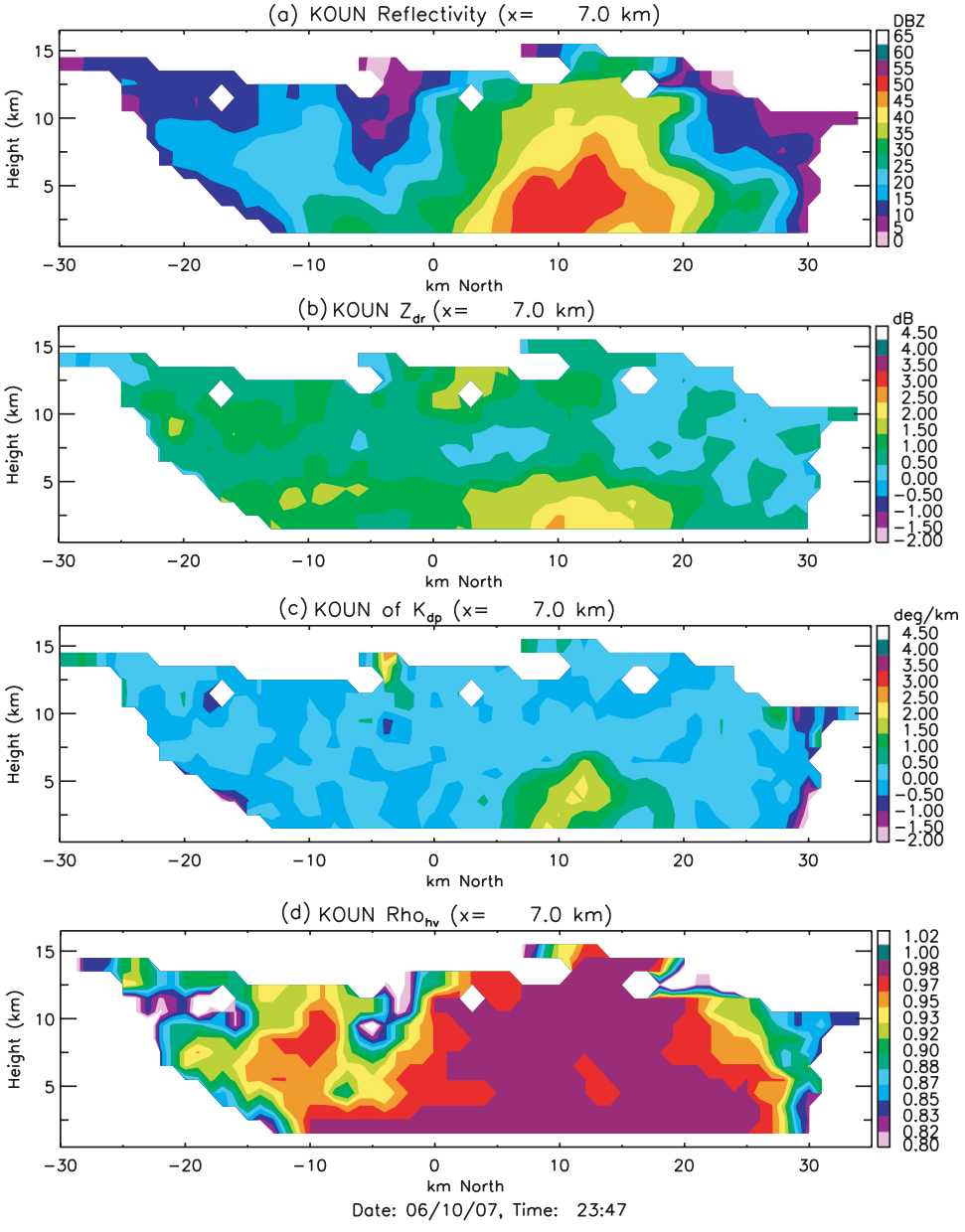

FIG. 7. As in Fig. 5, but for cross sections of (a) reflectivity, (b) Z_{dr}, (c) K_{dp}, and (d) ρ_{hv}.

variable ranges for seven different hydrometeor types, excluding hail and mixed-phase categories. S-band simulations were also performed for comparison. Many complex non-Rayleigh effects were seen at the shorter X-band wavelength, particularly in rain and graupel categories. Comparisons of simulated S-band ranges of variables were similar to reference S-band values given in the literature (S00), verifying that simulations were reasonable. Data from the CASA IP1 network were used to study the functionality of the new theory-based HID in comparison with a simple reflectivity and temperature HID, and results were also qualitatively evaluated against similar HID algorithms applied to S-band data from KOUN. It was shown that the S-band theory-based HID was similar to a currently employed S-band HID, lending some credence to the theory-based HID algorithms. The theory-based X-band algorithm seemed to perform relatively well and showed many similar microphysical characteristics to the S-band HIDs. The addition of aggregate and ice crystal categories to replace the CSUHID dry snow category assists in increasing the detail of microphysical processes. Because

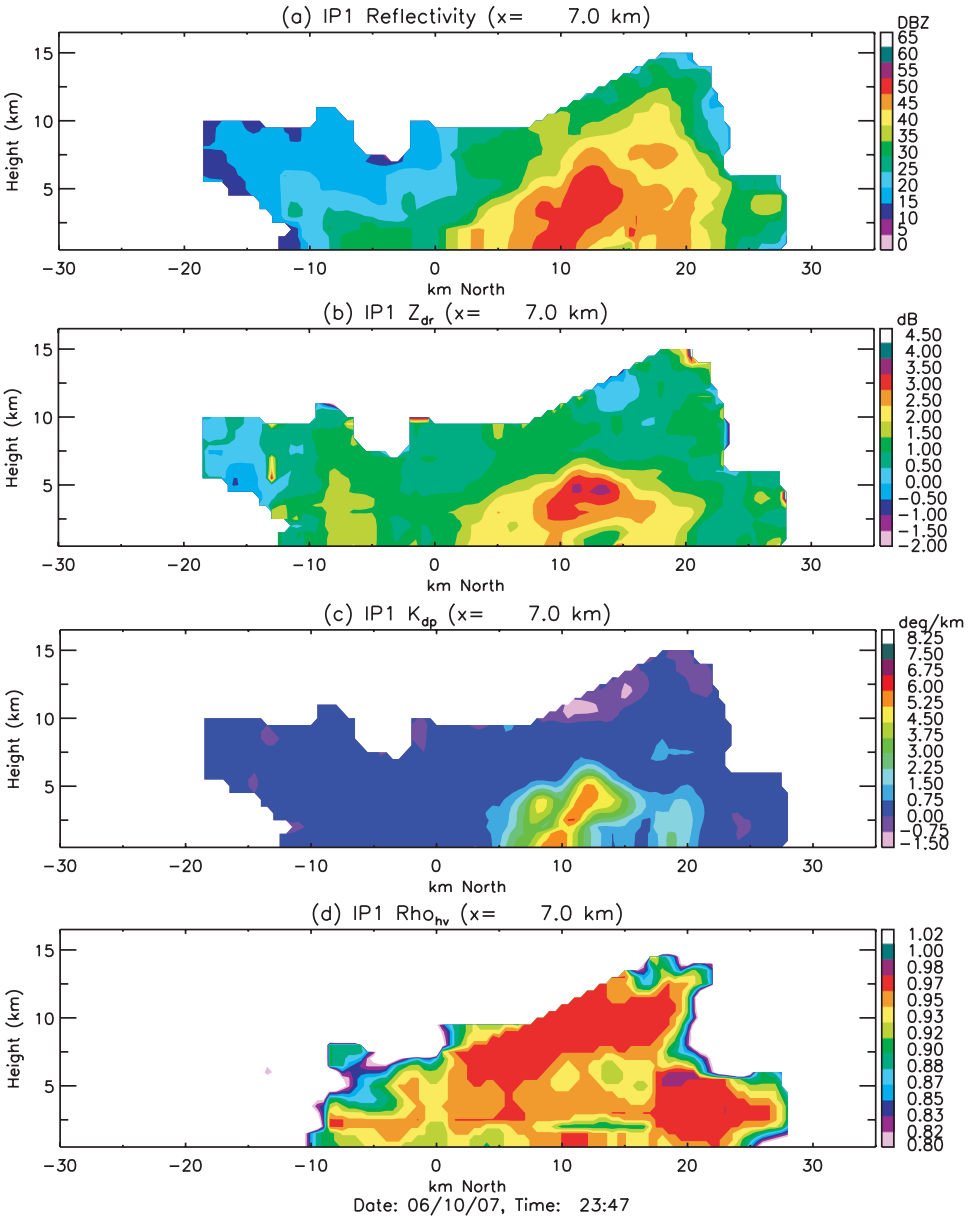

FIG. 8. As Fig. 6, but for cross sections of (a) reflectivity, (b) Z_{dr}, (c) K_{dp}, and (d) ρ_{hv}.

of lower confidence in IP1-measured Z_{dr} and ρ_{hv} during the case studied herein, the weights for these variables were decreased in the HID fuzzy-logic scoring. Nonetheless, comparisons with a simple fuzzy-logic reflectivity and temperature HID algorithm illustrated the value of microphysical information provided by the polarimetric variables in identifying rain above the melting layer, differentiating frozen hydrometeors such as graupel and aggregates, and enabling the distinction of vertically aligned ice crystals. Improved polarimetric quality would no doubt lead to higher confidence in the HID classifications and would likely lead to greater differences between nonpolarimetric and polarimetric-based HIDs. Future work will include applying the X-band theory-based HID to a number of different datasets and radars to test the robustness of the algorithm, as well as verification against in situ observations and cloud modeling when available. Further investigation of hail and mixed-phase categories for the X-band HID is also necessary.

Acknowledgments. The authors thank Prof. Chandrasekar and Dr. Y. Wang (both at Colorado State University) for assistance with data collection and interpretation, as well as the entire CASA IP1 team.

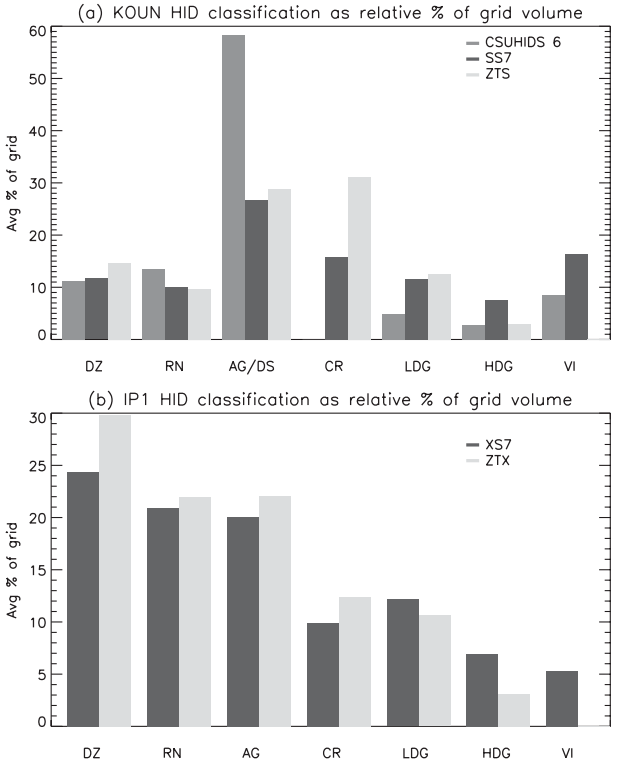

FIG. 9. Relative percentage of storm grid volume classified as each hydrometeor type through the lifetime of the 10 Jun 2007 storm using (a) KOUN and (b) IP1 HIDs.

Dr. S. Lim (CSU) furnished the network-based corrected reflectivity for the IP1 data. Dr. T. Schuur at NSSL provided KOUN data for the case study. This work is supported primarily by the Engineering Research Centers Program of the National Science Foundation under NSF Award 0313747, Colorado State University, and University of Massachusetts Contract UM04-002341.

REFERENCES

Auer, A. H., Jr., 1972: Distribution of graupel and hail with size. *Mon. Wea. Rev.,* **100,** 325–328.

Aydin, K., and T. A. Seliga, 1984: Radar polarimetric backscattering properties of conical graupel. *J. Atmos. Sci.,* **41,** 1887–1892.

Balakrishnan, N., and D. S. Zrnic, 1990: Use of polarization to characterize precipitation and discriminate large hail. *J. Atmos. Sci.,* **47,** 1525–1540.

Baldini, L., E. Gorgucci, V. Chandrasekar, and W. Peterson, 2005: Implementations of CSU hydrometeor classification scheme for C-band polarimetric radars. Preprints, *32nd Int. Conf. on Radar Meteorology,* Albuquerque, NM, Amer. Meteor. Soc., P11.4. [Available online at http://ams.confex.com/ams/pdfpapers/95865.pdf.]

Barber, P., and C. Yeh, 1975: Scattering of electromagnetic waves by arbitrarily shaped dielectric bodies. *Appl. Opt.,* **14,** 2864–2872.

Barthazy, E., and R. Schefold, 2003: Properties of snowflakes of different riming degree and crystal types. Preprints, *31st Int. Conf. on Radar Meteorology,* Seattle, WA, Amer. Meteor. Soc., 124–127. [Available online at http://ams.confex.com/ams/pdfpapers/64326.pdf.]

Battan, L. J., 1973: *Radar Observation of the Atmosphere*. The University of Chicago Press, 323 pp.

Beard, K. V., and A. R. Jameson, 1983: Raindrop canting. *J. Atmos. Sci.,* **40,** 448–454.

——, and C. Chuang, 1987: A new model for the equilibrium shape of raindrops. *J. Atmos. Sci.,* **44,** 1509–1524.

Braham, R. R., Jr., 1963: Some measurements of snow pellet bulk-densities. *J. Appl. Meteor.,* **2,** 498–500.

Brandes, E. A., G. Zhang, and J. Vivekanandan, 2002: Experiments in rainfall estimation with a polarimetric radar in a subtropical environment. *J. Appl. Meteor.,* **41,** 674–685.

——, K. Ikeda, G. Zhang, M. Schenhuber, and R. M. Rasmussen, 2006: A statistical and physical description of hydrometeor distributions in Colorado snow storms using a video disdrometer. *J. Appl. Meteor.,* **46,** 634–650.

Bringi, V. N., and V. Chandrasekar, 2001: *Polarimetric Doppler Weather Radar Principals and Applications*. Cambridge University Press, 656 pp.

Carey, L. D., and S. A. Rutledge, 1998: Electrical and multiparameter radar observations of a severe hailstorm. *J. Geophys. Res.,* **103,** 13 979–14 000.

Chandrasekar, V., and S. Lim, 2008: Retrieval of reflectivity in a networked radar environment. *J. Atmos. Oceanic Tech.,* **25,** 1755–1767.

——, ——, and E. Gorgucci, 2006: Simulation of X-band rainfall observations from S-band radar data. *J. Atmos. Oceanic Technol.,* **23,** 1195–1205.

——, D. McLaughlin, J. Brotzge, M. Zink, B. Philips, and Y. Wang, 2008: Evaluation of distributed collaborative sending in a four-node radar network: Integrated project 1. Preprints, *28th Int. Geoscience and Remote Sensing Symp. (IGARRS),* Boston, MA, IEEE, Vol. 5, 148–151.

Cheng, L., and M. English, 1983: A relationship between hailstone concentration and size. *J. Atmos. Sci.,* **40,** 204–213.

Chuang, C. C., and K. V. Beard, 1990: A numerical model for the equilibrium shape of electrified raindrops. *J. Atmos. Sci.,* **47,** 1374–1389.

Doviak, R. J., and D. S. Zrnic, 1993: *Doppler Radar and Weather Observations*. Academic Press, 562 pp.

Field, P. R., 1999: Aircraft observations of ice crystal evolution in an altostratus cloud. *J. Atmos. Sci.,* **56,** 1925–1941.

Fletcher, N. H., 1962: *The Physics of Clouds*. 2nd ed. Clarendon Press, 671 pp.

Goddard, J. W. F., and S. M. Cherry, 1984: Quantitative precipitation measurements with dual linear polarisation radar. Preprints, 22nd Int. Conf. on Radar Meteorology, Zurich, Switzerland, Amer. Meteor. Soc., 352–357.

Gunn, K. L. S., and J. S. Marshall, 1958: The distribution with size of aggregate snowflakes. *J. Atmos. Sci.,* **15,** 452–461.

Heymsfield, A. J., 1972: Ice crystal terminal velocities. *J. Atmos. Sci.,* **29,** 1348–1357.

——, 1978: The characteristics of graupel particles in northeastern Colorado cumulus congestus clouds. *J. Atmos. Sci.,* **35,** 284–295.

——, A. Bansemer, C. Schmitt, C. Twohy, and M. R. Poellot, 2004: Effective ice particle densities derived from aircraft data. *J. Atmos. Sci.,* **61,** 982–1003.

Hobbs, P. V., S. Chang, and J. D. Locatelli, 1974: The dimensions and aggregation of ice crystals in natural clouds. *J. Geophys. Res.,* **79,** 2199–2206.

Hogan, R. J., A. J. Illingworth, and H. Sauvageot, 2000: Measuring crystal size in cirrus using 35- and 94-GHz radars. *J. Atmos. Oceanic Technol.,* **17,** 27–37.

Jameson, A. R., 1983: Microphysical interpretation of multi-parameter radar measurements in rain. Part I: Interpretation of polarization measurements and estimation of raindrop shapes. *J. Atmos. Sci.,* **40,** 1792–1802.

Lim, S., 2001: Fuzzy logic system for hydrometeor classification from polarimetric radar measurements. M.S. thesis, Colorado State University, 97 pp.

——, V. Chandrasekar, and V. N. Bringi, 2005: Hydrometeor classification system using dual-polarization radar measurements: Model improvements and in situ verification. *IEEE Trans. Geosci. Remote Sens.,* **43,** 792–801.

List, R., 1958: Kennzzeichen atmosphärischer Eispartikeln, Part 1. *Z. Angew. Math. Phys.,* **9A,** 180–192.

——, and R. S. Schemenauer, 1971: Free-fall behavior of planar snow crystals, conical graupel and small hail. *J. Atmos. Sci.,* **28,** 110–115.

Liu, H., and V. Chandrasekar, 2000: Classification of hydrometeors based on polarimetric radar measurements: Development of fuzzy logic and neuro-fuzzy systems, and in situ verification. *J. Atmos. Oceanic Technol.,* **17,** 140–164.

Locatelli, J. D., and P. V. Hobbs, 1974: Fall speeds and masses of solid precipitation particles. *J. Geophys. Res.,* **79,** 2185–2197.

Magono, C., 1954: On the falling velocity of solid precipitation elements. *Sci. Pre. Yokohama Nat. Univ.,* **3,** 33–40.

Matrosov, S. Y., R. F. Reinking, R. A. Kropfli, and B. W. Bartram, 1996: Estimation of ice hydrometeor types and shapes from radar polarization measurements. *J. Atmos. Oceanic Technol.,* **13,** 85–96.

——, R. Cifelli, P. C. Kennedy, S. W. Nesbitt, S. A. Rutledge, V. N. Bringi, and B. E. Martner, 2006: A comparative study of rainfall retrievals based on specific differential phase shifts at X- and S-band radar frequencies. *J. Atmos. Oceanic Technol.,* **23,** 952–963.

McCormick, G. C., and A. Hendry, 1974: Polarization properties of transmission through precipitation over a communication link. *J. Rech. Atmos.,* **8,** 175–187.

Ono, A., 1970: Growth mode of ice crystals in natural clouds. *J. Atmos. Sci.,* **27,** 649–658.

Park, S.-G., V. N. Bringi, V. Chandrasekar, M. Maki, and K. Iwanami, 2005: Correction of radar reflectivity and differential reflectivity for rain attenuation at X band. Part I: Theoretical and empirical basis. *J. Atmos. Oceanic Technol.,* **22,** 1621–1632.

Pruppacher, H. R., and K. V. Beard, 1970: A wind tunnel investigation of the internal circulation and shape of water drops falling at terminal velocity in air. *Quart. J. Roy. Meteor. Soc.,* **96,** 247–256.

——, and R. L. Pitter, 1971: A semi-empirical determination of the shape of cloud and rain drops. *J. Atmos. Sci.,* **28,** 86–94.

——, and J. D. Klett, 1997: *Microphysics of Clouds and Precipitation*. 2nd ed. Kluwer Academic, 954 pp.

Rogers, D. C., 1974: Observational study of aggregation. *Bull. Amer. Meteor. Soc.,* **55,** 676.

Rottner, D., and G. Vali, 1974: Snow crystal habit at small excesses of vapor density over ice saturation. *J. Atmos. Sci.,* **31,** 560–569.

Ryzhkov, A. V., and D. S. Zrnic, 1998: Discrimination between rain and snow with a polarimetric radar. *J. Appl. Meteor.,* **37,** 1228–1240.

——, and ——, 2005: Radar polarimetry at S, C, and X bands comparative analysis and operational implications. Preprints, *32nd Conf. on Radar Meteorology,* Albuquerque, NM, Amer. Meteor. Soc., 9R.3. [Available online at http://ams.confex.com/ams/pdfpapers/95684.pdf.]

——, ——, and B. A. Gordon, 1998: Polarimetric method for ice water content determination. *J. Appl. Meteor.,* **37,** 125–134.

——, T. J. Schuur, D. W. Burgess, P. L. Heinselman, S. E. Giangrande, and D. S. Zrnic, 2005: The Joint Polarization Experiment: Polarimetric rainfall measurements and hydrometeor classification. *Bull. Amer. Meteor. Soc.,* **86,** 809–824.

Sekhon, R. S., and R. C. Srivastava, 1970: Snow size spectra and radar reflectivity. *J. Atmos. Sci.,* **27,** 299–307.

Straka, J. M., D. S. Zrnic, and A. V. Ryzhkov, 2000: Bulk hydrometeor classification and quantification using polarimetric radar data: Synthesis of relations. *J. Appl. Meteor.,* **39,** 1341–1372.

Tessendorf, S. A., L. J. Miller, K. C. Wiens, and S. A. Rutledge, 2005: The 29 June 2000 supercell observed during STEPS. Part I: Kinematics and microphysics. *J. Atmos. Sci.,* **62,** 4127–4150.

Tian, L., G. M. Heymsfield, and R. C. Srivastava, 2002: Measurement of attenuation with airborne and ground-based radar in convective storms over land and its microphysical implications. *J. Appl. Meteor.,* **41,** 716–733.

Ulbrich, C. W., 1983: Natural variations in the analytical form of the raindrop size distribution. *J. Climate Appl. Meteor.,* **22,** 1764–1775.

Vivekanandan, J., W. M. Adams, and V. N. Bringi, 1991: Rigorous approach to polarimetric radar modeling of hydrometeor distributions. *J. Appl. Meteor.,* **30,** 1053–1063.

——, D. S. Zrnic, S. M. Ellis, R. Oye, A. V. Ryzhkov, and J. Straka, 1999: Cloud microphysics retrieval using S-band dual-polarization radar measurements. *Bull. Amer. Meteor. Soc.,* **80,** 381–388.

Weinheimer, A. J., and A. A. Few, 1987: The electric field alignment of ice particles in thunderstorms. *J. Geophys. Res.,* **92,** 14 833–14 844.

Willis, P. T., 1984: Functional fits to some observed drop size distributions and parameterization of rain. *J. Atmos. Sci.,* **41,** 1648–1661.

——, and A. J. Heymsfield, 1989: Structure of the melting layer in mesoscale convective system stratiform precipitation. *J. Atmos. Sci.,* **46,** 2008–2025.

Xu, J. L., 1983: Some hail research in China. *Bull. Amer. Meteor. Soc.,* **64,** 124–129.

Zikmunda, J., and G. Vali, 1972: Fall patterns and fall velocities of rimed ice crystals. *J. Atmos. Sci.,* **29,** 1334–1347.

Zrnic, D. S., A. Ryzhkov, J. Straka, Y. Liu, and J. Vivekanandan, 2001: Testing a procedure for automatic classification of hydrometeor types. *J. Atmos. Oceanic Technol.,* **18,** 892–913.